Chemical Engineering Journal 547 (2026) 181339

Contents lists available at ScienceDirect

Chemical Engineering Journal

journal homepage: www.elsevier.com/locate/cej

Dynamic interfacial polarization via electric double layer coupling in semiconductor–liquid–metal junctions for direct-current tribovoltaic nanogenerators

Sheng-Jie Lin [a,b,1], Jiang-Tao Guo [b,1], Xin-Long Xiao [a,b], Wen Yang [b], Yun-Bo Zhang [b], Yong Zhang [c], Pei-Zhi Yang [a,b,*]

[a] Yunnan Normal University, School of Energy and Environment Science, Southwest United Graduate School, No. 298, Yieryi Street, Kunming, Yunnan, 650092, China
[b] Yunnan Normal University, School of Energy and Environment Science, No. 768, Juxian Street, Chenggong District, Kunming, Yunnan, 650500, China
[c] Department of Electrical and Computer Engineering and Center for Optoelectronics, University of North Carolina at Charlotte, Charlotte, NC, 28223, USA

ARTICLE INFO

Keywords:
Tribovoltaic effect
Electric double layer
Solid-liquid-solid Interface
Direct-current triboelectric Nanogenerator
Flexible power source

ABSTRACT

Conventional droplet-type tribovoltaic nanogenerators (TVNGs) are inherently restricted by open interfaces and intermittent droplet operation, where erratic solid-liquid contact and excessive interfacial charge dissipation drastically degrade their direct-current (DC) output and operational stability. In this work, we report a fully enclosed solid-liquid-solid (S-L-S) DC generator, termed an electric double layer induced semiconductor non-equilibrium triboelectric nanogenerator (EDL-SNE-TENG). Within this confined system, an ultrathin water film establishes two parallel and coupled electric double layers at the water-silicon and water-silver interfaces. Under cyclic mechanical compression, reversible polarization and ordered arrangement of interfacial water molecules are induced, reducing the effective work function of silicon to 4.02 eV. The dynamically polarized interface generates an intense localized electric field that continuously reduces the effective resistance to interfacial charge transfer and facilitates the directional transport of non-equilibrium charge carriers. This polarization-enhanced tribovoltaic effect enables highly efficient directional charge migration. The optimized EDL-SNE-TENG delivers an open-circuit voltage of 6.5 V, a short-circuit current of 35 μA, and a power density of 0.54 $W{\cdot}m^{-2}$, exhibiting a 50-fold enhancement in peak power density over conventional TVNGs. This work provides a theoretical foundation for fluidic-gating-enabled DC energy harvesting and a rectifier-free route toward practical self-powered devices.

1. Introduction

The rapid development of Internet of Things (IoT) devices, wearable electronics and human-machine interaction systems has fueled an increasing demand for reliable micro-energy solutions, positioning self-powered technologies as a promising route toward sustainable device operation. Liquid-solid triboelectric nanogenerators (LS-TENGs) can effectively harvest mechanical energy from flowing water and falling droplets, exhibiting substantial potential for powering low-consumption microdevices [1,2]. However, conventional LS-TENGs operate based on contact electrification and electrostatic induction, inherently generating alternating current (AC). Consequently, external rectification circuits are indispensable for achieving direct-current (DC) output, which inevitably increases device size and energy consumption, thereby limiting system integration and practical application [3–5].

The tribovoltaic effect offers a different solution to this challenge by enabling the direct generation of directional charge carriers at solid-liquid interfaces, thereby allowing rectifier-free DC output and facilitating the development of simplified, high-performance nanogenerators. Despite these advantages, most existing tribovoltaic nanogenerators (TVNGs) rely on open interfaces and discrete droplet operation, which introduce several inherent drawbacks that severely restrict their output performance and practical utility [6–14]. First, each droplet-solid contact lasts only several milliseconds, which is too brief for sufficient

* Corresponding author at: Yunnan Normal University, School of Energy and Environment Science, Southwest United Graduate School, No. 298, Yieryi Street, Kunming, Yunnan, 650092, China.
E-mail address: pzhyang@hotmail.com (P.-Z. Yang).
[1] These authors contributed equally.

https://doi.org/10.1016/j.cej.2026.181339
Received 29 June 2026; Received in revised form 6 August 2026; Accepted 28 August 2026
Available online 31 August 2026

charge transfer and results in low energy collection efficiency per working cycle [15,16]. Second, the intrinsically stochastic nature of droplet impact leads to unstable contact areas, variable contact pressure and uncertain contact angles. These unregulated interfacial conditions produce inconsistent electrical output and poor signal repeatability. Third, open systems suffer from severe charge dissipation. A substantial portion of accumulated interfacial charges is removed along with departing droplets, causing significant energy loss. Owing to these limitations, conventional open-interface TVNGs exhibit weak output performance, with open-circuit voltages below 1.0 V, microampere-level short-circuit currents, and peak power densities lower than 0.01 $W{\cdot}m^{-2}$ [17–27]. Such performance remains inadequate for driving most practical microelectronic devices.

To overcome these challenges, we herein present a fully enclosed solid-liquid-solid (S-L-S) DC nanogenerator, termed an electric double layer induced semiconductor non-equilibrium triboelectric nanogenerator (EDL-SNE-TENG). Unlike conventional devices relying on discrete droplets, this enclosed configuration employs a continuous ultrathin water film to maintain stable solid-liquid contact under cyclic compression. This structural design effectively suppresses random contact fluctuation and interfacial charge loss, while the coupled electric double layers at the interfaces enable efficient charge retention and directional migration. Under mechanical compression, reversible molecular polarization reduces the effective work function of silicon to 4.02 eV and triggers dynamic fluidic gating, which changes the interfacial potential distribution, reduces the effective resistance to interfacial charge transfer, and facilitates the directional transport of non-equilibrium carriers for enhanced tribovoltaic output. The fabricated EDL-SNE-TENG achieves stable rectifier-free DC output with an open-circuit voltage of 6.5 V, a short-circuit current of 35 μA and a peak power density of 0.54 $W{\cdot}m^{-2}$, representing over 50-fold performance improvement compared with traditional TVNGs. This work explores interfacial polarization and non-equilibrium charge evolution at water-semiconductor interfaces, providing new insights and a viable design strategy for fluidic-gated DC self-powered systems.

2. Experimental section

2.1. Fabrication of the EDL-SNE-TENG device

A commercially available n-type silicon (100) wafer (resistivity 1–3 Ω·cm, thickness 500 μm) was selected as the functional backbone. Prior to device assembly, the Si wafer underwent a standard RCA cleaning protocol to eliminate organic residues, metallic impurities, and native oxides, ensuring an atomically clean interface for subsequent modifications.

Following surface texturing, a highly conductive Ag electrode layer (thickness ~ 200 nm) was deposited onto the rear unpolished side of the n-Si wafer using Multi-Source Deposition System (MIKROUNA Shanghai Company). The comprehensive deposition parameters, including base pressure, rate, and post-annealing conditions to ensure ohmic contact, are fully specified in Table S1. The ohmic nature of the Ag/n-Si contact is confirmed by the linear current-voltage (I-V) characteristic measured under completely dry conditions in a dual-bottom-electrode configuration, where the current flows exclusively through the Ag/n-Si/Ag path. This back electrode ensures an ohmic contact for efficient charge collection. To define the active interaction region, the central area of the textured n-Si surface was selectively treated with oxygen plasma (100 W, 60 s, 20 sccm O_2, 10 Pa) to generate surface hydroxyl groups, rendering it super-hydrophilic with a static contact angle of approximately 30°. This hydrophilic anchor point is critical for stabilizing the water droplet dynamics during mechanical compression. Conversely, a commercially available polytetrafluoroethylene (PTFE) film (thickness: 0.2 mm) served as the tribo-negative dielectric layer. The PTFE surface facing the water droplet was also lightly treated to optimize its electret properties and surface energy for consistent contact electrification. The EDL-SNE-TENG assembly was completed by encapsulating the edges with an insulating acrylic spacer to maintain structural integrity while allowing the free vertical displacement of the PTFE film.

2.2. Characterization and measurement

The surface morphology and microstructural features of the textured n-Si substrate and the deposited Ag electrode were systematically characterized using a Field Emission Scanning Electron Microscope (SEM, Thermo Fisher Scientific) operating at an accelerating voltage of 5 kV. The elemental composition and purity of the silicon substrate were verified via Energy Dispersive X-ray Spectroscopy (EDS) mapping. The wetting behaviors of the solid surfaces were evaluated by measuring the static contact angles of deionized (DI) water droplets (5 μL) using a commercial contact angle goniometer (JY-82B Kruss DSA) under ambient conditions.

2.3. Electrical performance assessment

To evaluate the energy harvesting performance, the EDL-SNE-TENG was mounted on a programmable linear motor platform (LHR14S Antek Automation Technology (Suzhou) Co., Ltd.), which provided precise control over the mechanical compression frequency, amplitude, and force. A periodic contact-separation motion was applied to the PTFE film against the water-droplet/n-Si interface at a standard frequency of 5 Hz unless otherwise specified. The experimental setup and the corresponding pressure and current responses under cyclic mechanical loading are shown in Fig. S1. DI water (resistivity 18.2 MΩ·cm) was employed as the standard liquid medium, with comparative tests conducted using tap water to assess environmental robustness.

The electrical output signals, including open-circuit voltage (V_{oc}), short-circuit current (I_{sc}), and transferred charge (Q_{tr}), were acquired in real-time using a high-impedance electrometer (Keithley 6514) connected to a computer-controlled data acquisition system. The sampling rate was set to sufficiently capture the transient DC pulse characteristics. The output power density was characterized by connecting variable external load resistors (ranging from 100 Ω to 1 GΩ) in series with the EDL-SNE-TENG and measuring the voltage drop across the load. All electrical measurements were conducted in a shielded Faraday cage to minimize external electromagnetic interference, under controlled environmental conditions (Temperature: 25 ± 1 °C, Relative Humidity: 40% ± 5%).

3. Results and discussion

3.1. Structural design and configuration of the EDL-SNE-TENG

As illustrated in Fig. 1a, the structural configuration of the proposed EDL-SNE-TENG features a typical solid-liquid-solid multiphase heterostructure. An n-type silicon wafer serves as the functional semiconductor substrate, with a silver layer sputtered on its rear surface to form a stable ohmic contact. The morphology and dimensional characteristics of the n-Si substrate and silver electrode are provided in Figs. S2 and S3. Scanning electron microscopy observations reveal a uniform micro-nano textured morphology on the silicon surface (Fig. 1a, inset i). This textured structure enlarges the specific surface area, which is beneficial for interfacial charge trapping and for regulating surface wetting behavior. Although crystalline silicon inherently contains defects that may promote carrier recombination, the fabricated device still sustains a stable DC output. This observation indicates that charge separation in this system is predominantly governed by the dynamic solid-liquid interface. Specifically, the interfacial electric field is sufficiently strong to rapidly sweep out non-equilibrium carriers before recombination can occur, thereby rendering the device tolerant to certain intrinsic semiconductor defects. The dynamic interfacial interaction under periodic mechanical excitation governs the operating behavior of the S-L-S

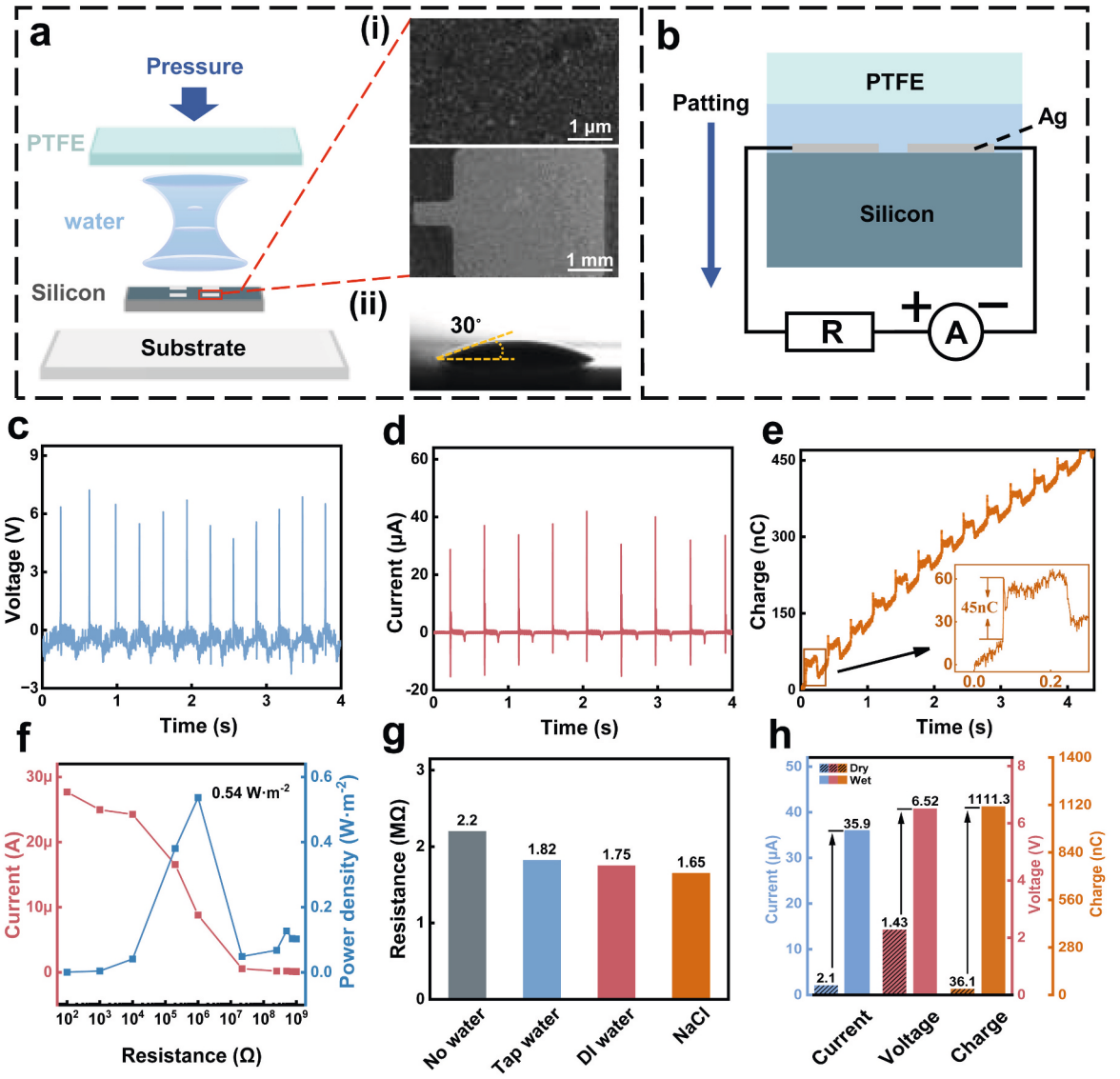

Fig. 1. (a) Schematic of the EDL-SNE-TENG based on an S-L-S heterostructure (Insets show SEM images of the textured n-Si surface and Ag electrode, and an optical image of a water droplet on the super-hydrophilic n-Si surface). (b) Equivalent circuit of the measurement setup. (c-e) Open-circuit voltage, short-circuit current, and transferred charge per cycle under 5 Hz compression. (f) Output power density versus load resistance. (g) Steady-state resistance for different liquid media. (h) Comparison of peak short-circuit current, open-circuit voltage, and per-cycle transferred charge under dry and wet conditions.

heterostructure, as depicted in Fig. S4. To stabilize liquid distribution and ensure consistent interfacial contact, the silicon surface was selectively treated to maintain a clean hydrophilic state with a contact angle of approximately 30° (Fig. 1a, inset ii). The change in wettability following plasma treatment is summarized in Table S2. Such hydrophilic modification enables uniform and stable spreading of the ultrathin water film, which is essential for reliable and efficient energy harvesting. The influence of PTFE thickness on electromechanical coupling performance was also investigated, with detailed parametric optimization presented in Table S3. For device assembly, a tiny droplet of deionized water was deposited on the pretreated n-Si surface, followed by coverage with a PTFE film. The resulting ultrathin water film serves as a flexible intermediate layer that bridges the PTFE film and the semiconductor substrate, forming a configuration fundamentally distinct from conventional dry-contact or open-interface designs.

The electrical measurement setup is shown in Fig. 1b, where the silver back electrode and an external load were connected to a Keithley 6514 electrometer for signal acquisition. Periodic mechanical compression at 5 Hz was applied to the PTFE top surface to induce cyclic interfacial compression and relaxation. Both n-Si and PTFE surfaces were modified by plasma treatment to improve hydrophilicity and enhance solid-liquid interfacial coupling. The band evolution behavior at the Ag/n-Si junction under different wetting conditions is illustrated in Fig. S5, revealing the underlying field modulation mechanism during device operation. Under weak wetting conditions (contact angle ≈ 60°) corresponding to initial contact state, water adsorption on the silicon surface is limited, and the n-Si substrate maintains a relatively high work function. After the Ag/n-Si contact is established, interfacial charge redistribution occurs until equilibrium is reached. Under weak-wetting conditions, limited water adsorption results in a relatively high effective resistance to interfacial charge transfer. When the surface transitions to a fully hydrophilic state (contact angle ≈ 30°), a continuous water film forms and generates interfacial EDLs. The adsorbed water dipoles reduce the effective work function of n-Si. Although the work function difference between n-Si and Ag decreases, the potential drop introduced by the EDL acts as an additional gating effect, which modifies the interfacial potential distribution and reduces the effective resistance to charge transfer, thereby improving charge separation and transport

efficiency. Under repeated mechanical compression, the increasingly ordered interfacial water dipoles progressively reduce the effective work function of n-Si, which finally stabilizes at approximately 4.02 eV. In this state, the EDL field cooperates with the dynamic triboelectric potential at the solid-liquid interface, thereby increasing the interfacial charge density and strengthening the dynamic charging effect.

The enhanced accumulation of anions near the water/n-Si interface increases the surface hole concentration and forms more electrostatically coupled anion-hole pairs. This process changes the surface potential of n-Si and establishes a transient potential difference between n-Si and the Ag electrodes. To restore charge equilibrium, electrons migrate toward the Ag electrodes, facilitating directional non-equilibrium carrier transport and ultimately yielding optimized electrical output performance (Fig. S6). The optimized EDL-SNE-TENG demonstrates superior electrical performance under periodic excitation. As shown in Fig. 1c-d, the device generates typical DC pulse signals, achieving a V_{oc} of approximately 6.5 V and an I_{sc} of 35 μA. The accumulated transferred charge per cycle reaches 45 nC (Fig. 1e), a value significantly surpassing those of conventional L-S TENG systems, thereby highlighting the superior charge management capability of the S-L-S architecture. Power characterization (Fig. 1f) indicates a peak power density of 0.54 $W{\cdot}m^{-2}$ under optimal load matching, demonstrating its potential for driving micro-electronic devices. Comparative investigations further reveal that the EDL-SNE-TENG performance is insensitive to the ionic strength of the liquid medium, with tap water and deionized water yielding comparable outputs (Fig. S7).

Parametric optimization confirms that a PTFE layer of 0.2 mm thick yields the maximum current output (Fig. S8). The Ag electrode spacing was further optimized using spacings of 4, 6, 8, and 10 mm (Fig. S9). With increasing electrode spacing, the output current decreased while the interelectrode resistance increased; therefore, 4 mm was selected for subsequent measurements. Comparative tests using different liquid media verify that the intermediate water film provides effective conductive coupling (Fig. 1g). A quantitative performance comparison under dry and wet operating conditions is summarized in Fig. 1h. The introduction of the interfacial water film increases the short-circuit current by approximately 17.1 times, the open-circuit voltage by 4.6 times, and the single-cycle transferred charge by 30.8 times. Substrate comparison experiments further demonstrate that n-Si exhibits superior output performance compared with other semiconductor and insulating materials (Fig. S10), underscoring the indispensable role of semiconductor band modulation in the energy conversion process. Single-electrode control tests (Fig. S11) also verify that both the water intermediate layer and the PTFE film are required to achieve efficient energy conversion. The performance of the EDL-SNE-TENG is compared with recently reported liquid-solid nanogenerators in Table S4. Operational durability is essential for the practical application of TENGs [28]. To verify this, the representative current signals before and after cycling, along with the long-term output response (Fig. S12), demonstrate that the device maintains a sustained electrical output without obvious degradation.

Collectively, these experimental results consistently confirm that the synergistic effect between electric double layer coupling and fluidic gating dominates the interfacial charge behavior, enabling the EDL-SNE-TENG to achieve high-performance, rectifier-free DC output.

3.2. *Universality study of the DC droplet generator based on semiconductor non-equilibrium effects induced by water-solid interfacial contact electrification*

To reveal the fundamental electrical distinction between the proposed water-bridge coupling mechanism and conventional solid-solid contact designs, four interfacial configurations with corresponding equivalent circuit models were designed and compared (Fig. 2a and

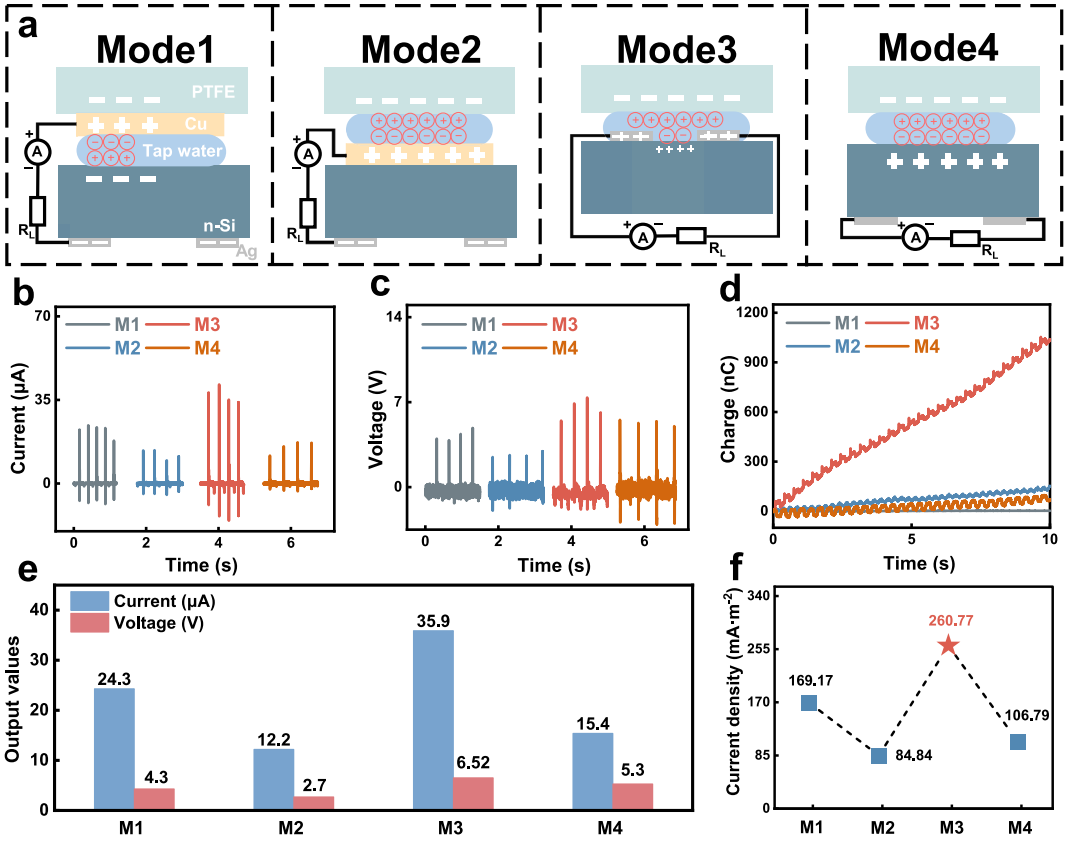

Fig. 2. (a) Schematics of the four generator modes. (b-d) Comparison of short-circuit current, open-circuit voltage, and transferred charge among the four modes. (e) Summary of output performance metrics. (f) Instantaneous current density signals.

Fig. S13). The four modes are defined as follows. In Mode 1, a copper foil was attached to the back of a PTFE film, and the assembly was placed onto an n-Si substrate. In this configuration, the water droplet bridges only the copper foil and the n-Si surface. In Mode 2, a copper foil was attached to the top surface of an n-Si substrate with a bottom silver electrode, and the water droplet contacted only the copper foil. Mode 3 corresponds to the proposed EDL-SNE-TENG configuration. Without any copper foil, the silver electrode was directly patterned on the top surface of the n-Si substrate, enabling the water droplet to simultaneously contact the PTFE layer, the n-Si surface, and the silver electrode. This constitutes the core device structure of the present work. Mode 4 was modified from Modes 1 and 2 by removing the copper foil component. Mode 1 operates based on contact-induced electrostatic induction. Energy conversion is achieved via periodic contact and separation between the water droplet and the bottom electrode, which forms capacitive coupling with the top dielectric PTFE layer. Mechanical motion disrupts the electrostatic equilibrium and triggers interfacial charge transfer. However, two key factors constrain its output performance. First, the fixed contact area of 1.44 mm^2 between the water droplet and the n-Si introduces considerable parasitic capacitance, denoted as $C_{W/N}$. According to the equivalent circuit and the equation $V_{OC} = Q/C_{W/N}$ [29], this parasitic capacitance produces a shunting effect that suppresses the open-circuit voltage. Second, interfacial charge induction and transfer proceed continuously rather than instantaneously. Although this structure can achieve energy conversion, its voltage and current output remain low. Thus, the performance limitation originates from the device output configuration and parasitic capacitance effect, rather than from insufficient interfacial charge generation. Consequently, Mode 1 was adopted as the baseline control to clarify the optimization direction for electrode design and parasitic capacitance suppression. Mode 2 shares a similar working principle with Mode 1, but with the copper electrode placed directly on the n-Si surface. This forms a polymer-water-metal sandwiched interface, where electric double layers primarily form at the PTFE-water and PTFE-Cu interfaces. In this configuration, the built-in electric field of the semiconductor barely contributes to charge regulation.

Mode 4 follows an operating principle similar to that of Mode 3. However, with the silver electrode positioned at the bottom of the substrate, the induced electrical signal is substantially attenuated. Mode 3 represents the optimized configuration of the EDL-SNE-TENG. With the top-layer silver electrode on the n-Si, the circuit conducts immediately once the water droplet contacts both the n-Si surface and the silver electrode under PTFE compression. This structural design offers two prominent advantages. First, the water medium forms two parallel capacitances $2C_{W/A}$ and $C_{W/N}$ at the water-silver and water-semiconductor interfaces, respectively, which effectively restrains parasitic capacitance. Second, direct contact between water and both the n-Si and silver surfaces reduces the interfacial work function and increases the interfacial potential difference, thereby greatly boosting the output power. Figs. 2b-2f demonstrate that Mode 3 achieves the optimal performance, delivering a steady short-circuit current of 35 μA, an open-circuit voltage of 6.5 V, and the maximum single-cycle transferred charge. Such superior performance stems from the unique water-bridge coupling effect of the S-L-S heterostructure. The interfacial water film functions not merely as a passive ohmic channel but as a dynamic charge bridge between the silver electrode and the n-Si substrate. Mechanical compression drives directional alignment of water dipoles and generates localized electric double layers. The dynamically polarized EDL modifies the interfacial potential distribution and facilitates directional charge transfer at the semiconductor interface.

In contrast to Modes 1, 2 and 4, which are based on conventional solid-solid contact, the water film in the EDL-SNE-TENG actively regulates interfacial electrical behaviors rather than merely transferring charges. It dynamically modulates the interfacial work function and synergizes the transport of ions, electrons and holes. Mechanical compression induces an asymmetric EDL distribution at the solid–liquid interface, thereby modifying the interfacial potential distribution and promoting directional charge redistribution. At the dynamic level, it achieves high-efficiency charge transfer with suppressed parasitic capacitance. The quantitative comparison of peak voltage, current, power density and transferred charge among the four modes is summarized in Table S5, which validates both the structural and mechanistic superiority of the proposed EDL-SNE-TENG.

3.3. *Enhancement effect of interfacial water medium and charge transfer mechanism*

The improved electrical performance enabled by the interfacial water film is presented in Fig. 3a. Experimental results verify that the introduction of the interfacial water film greatly enhances the device output. Under wet conditions, the peak short-circuit current rises from 2.1 μA (under dry conditions) to 35.9 μA, while the open-circuit voltage increases from 1.43 V to 6.5 V (Fig. S14a). The total transferred charge within 10 s of continuous operation increases by a factor of 30.8 (Fig. S14b). This substantial performance improvement originates from the mechanical deformation of the water droplet, which disrupts the initial solid-liquid interfacial equilibrium and establishes an asymmetric ionic distribution. This process greatly enhances the interfacial charge separation efficiency. These observations demonstrate the essential role of water in facilitating charge separation, which is governed by the dynamic work function modulation at the solid-liquid interface [30]. Interfacial wettability was further characterized to elucidate the interfacial behavior of water molecules (Fig. S15). The PTFE surface exhibits hydrophobic characteristics with a contact angle of 101°, corresponding to weak solid-liquid adhesion. In comparison, the n-Si surface shows moderate hydrophilicity with a contact angle of 57°. Fig. S16 illustrates the molecular arrangement of interfacial water before and after mechanical compression. In the initial state without external pressure, water molecules between the n-Si substrate and the silver electrode are randomly distributed with disordered dipole orientations. Consequently, the resulting interfacial electric field is too weak to drive effective charge separation. Under mechanical compression, the confined water layer undergoes structural rearrangement. External pressure tightens the solid-liquid contact and forces water molecules into a highly ordered alignment with spatial asymmetry. At the positively charged n-Si interface, the oxygen atoms of water molecules orient toward the silicon surface. At the negatively charged Ag interface, the hydrogen atoms of water molecules orient toward the electrode surface [31]. The unified dipole orientation collectively builds a strong interfacial electric field directed from silver toward n-Si. This mechanically induced non-equilibrium field changes the interfacial potential distribution and reduces the effective resistance to interfacial charge transfer, providing a strong driving force for efficient charge separation and directional charge transport. Kelvin probe force microscopy (KPFM) measurements were conducted to validate the correlation between water molecular polarization and surface work function variation [32]. Dynamic characterization shown in Figs. 3b and S17, reveals that continuous mechanical cycling gradually reduces the n-Si surface work function. As the cycle number increases from 0 to 8, the work function decreases rapidly before the reduction slows down and finally stabilizes at 4.02 eV. This trend indicates that cyclic mechanical loading promotes continuous interfacial charge transfer and accumulation until a dynamic equilibrium is reached, forming a stable non-equilibrium field on the semiconductor surface. This steady state arises from the combined effect of mechanically induced triboelectric potential and solid-liquid electric double layer polarization. The observed dynamic interfacial electronic evolution arises from two cooperative factors. First, cyclic friction accumulates negative charges on the PTFE surface, generating an external electric field that enhances interfacial polarization and promotes the dynamic charging of the EDL. Second, repeated compression stabilizes the ordered arrangement of interfacial water dipoles and strengthens remnant polarization [33]. Once charge accumulation reaches

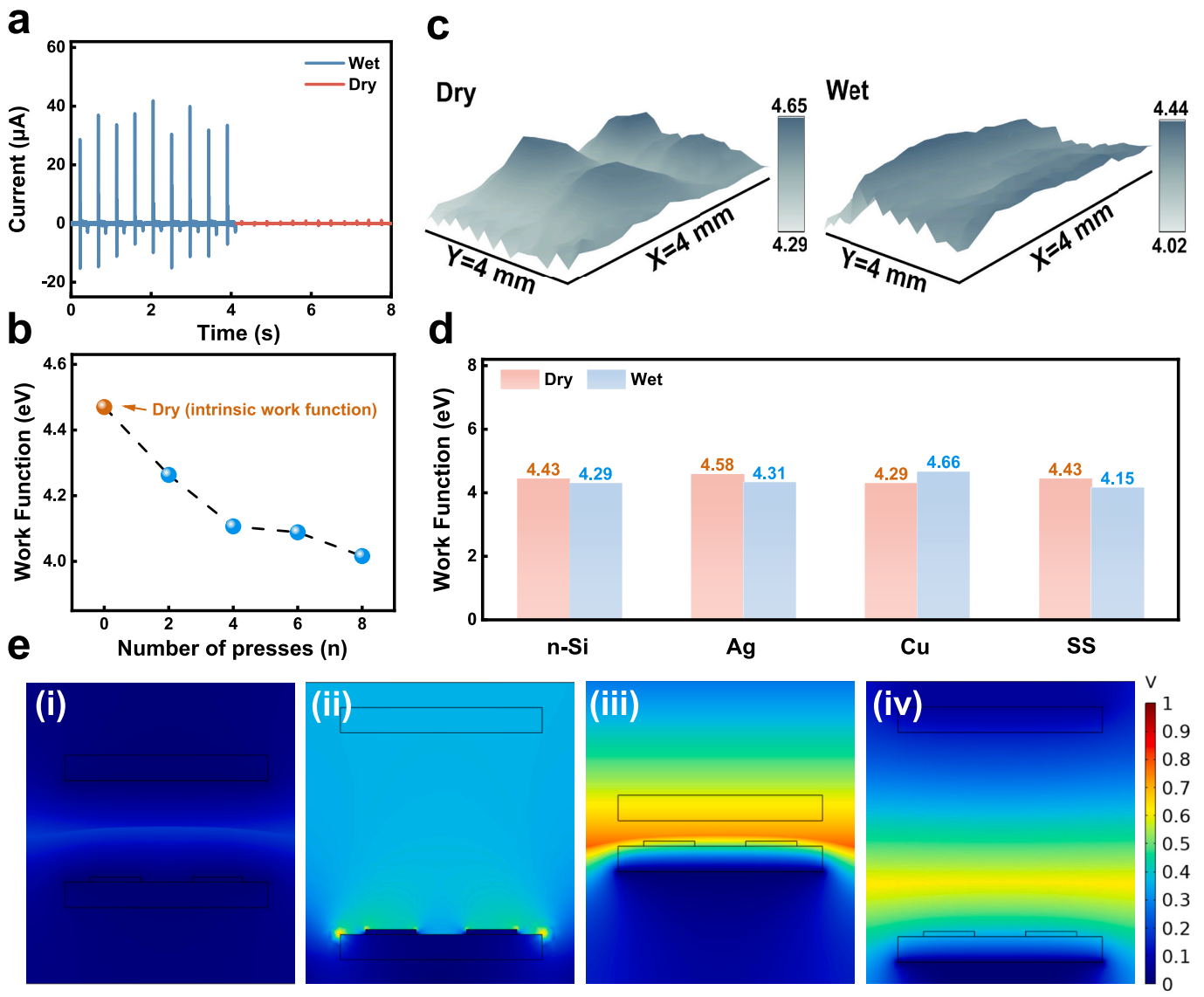

Fig. 3. (a) Comparison of output current with and without water. (b) Work function evolution of n-Si with contact cycles (c) Work function mapping of n-Si (eV). (d) Work function comparison of Si, Ag, Cu, and SS under dry and wet conditions (n-Si here refers to bare n-type silicon without Ag coating, SS stands for stainless steel). (e) COMSOL simulation of the device for one cycle.

equilibrium, the surface work function remains constant at 4.02 eV. Table S6 summarizes the corresponding surface potential and work function evolution under static and dynamic wet conditions. Static tests further reveal the intrinsic work function modulation induced by water adsorption. As shown in Fig. 3c, the silver-coated silicon surface exhibits an average work function of 4.47 eV in the dry state. After water film formation, the static equilibrium work function decreases to 4.23 eV, corresponding to a negative shift of 0.24 eV. This reduction demonstrates that water adsorption redistributes the interfacial charges and modifies the surface potential of n-Si, thereby strengthening the interfacial electric field [34]. Such interfacial modification serves as the fundamental prerequisite for the mechanically triggered non-equilibrium field effect. A similar work function reduction is also observed in p-Si, textured p-Si and textured n-Si (Fig. S18), indicating that water-induced work function lowering is a universal phenomenon for silicon-based surfaces [35]. Fig. 3d compares the work function variation of bare and silver-coated n-Si before and after wetting. Bare n-Si shows a work function decrease from 4.43 eV under dry conditions to 4.29 eV under wet conditions, consistent with the trend observed for silver-decorated n-Si. Finite element simulations (Fig. 3e) further corroborate the electric field distribution within the confined S-L-S structure under mechanical compression. The results show that the ordered alignment of interfacial water dipoles generates a strong localized electric field at the water-Si interface, which is sufficient to significantly reduce the semiconductor work function, in good agreement with the KPFM measurements presented above.

Statistical analysis based on 1000 sampling points from Fig. S19a further validates the universal work function reduction of Ag and Si surfaces after water coverage. Water adsorption induces interfacial charge redistribution at the Ag and Si surfaces, resulting in measurable changes in their surface potential and work functions. In contrast, copper exhibits an opposite trend. The lower electronegativity of copper (relative to water) drives electron transfer from the metal surface to water, forming positively charged surface sites and increasing the work function [36–38]. Dynamic measurements in Fig. S19b confirm that the copper work function gradually rises and stabilizes under cyclic compression. This variation arises from two factors. First, the inherent electronegativity difference between copper ($\chi \approx 1.9$) and water ($\chi \approx$ 2.5–3.0) creates a surface dipole layer that elevates the apparent work function. Second, the aqueous environment promotes surface oxidation

of copper, forming high-work-function Cu_2O (5.3 eV). This distinct behavior further proves that electrode material properties and electronegativity-governed charge transfer dominate interfacial electrical responses [39].

The influence of semiconductor doping concentration on interfacial modulation was also explored using n-Si substrates with different resistivities under identical wetting conditions, as shown in Fig. S20. A higher doping concentration reduces silicon resistivity and shifts the Fermi level closer to the conduction band, yielding a lower initial work function. After water film coverage, all samples exhibit negative work function shifts, and the magnitude of shift correlates closely with substrate resistivity. This demonstrates that semiconductor doping can effectively tailor the initial band-bending state, optimizing interfacial charge transfer behavior and electric double layer configuration during solid-liquid contact. These findings provide fundamental guidance for the interfacial field-effect design and performance modulation of EDL-SNE-TENG devices. Table S7 summarizes the opposite work function evolution of high-electronegativity materials (Ag, Si) and low-electronegativity Cu, which is consistent with the charge transfer direction predicted by the triboelectric series. Table S8 further compares the output performance of different substrates, including n-Si, p-Si and insulators, verifying the indispensable contribution of semiconductor non-equilibrium effects to high-performance DC energy conversion.

3.4. Multi-scale charge transfer mechanism and dynamic field effect modulation

The device initially remains in a stationary state, with the PTFE film separated from the water layer. Ag electrodes were deposited on the n-Si surface by electron-beam evaporation. Charge redistribution occurs at the Ag/n-Si interface until Fermi-level equilibrium is reached, while the ohmic behavior of the contact is confirmed by the linear I-V characteristic. When the water droplet simultaneously contacts n-Si and Ag, two parallel electric double layers form at the water/n-Si and water/Ag

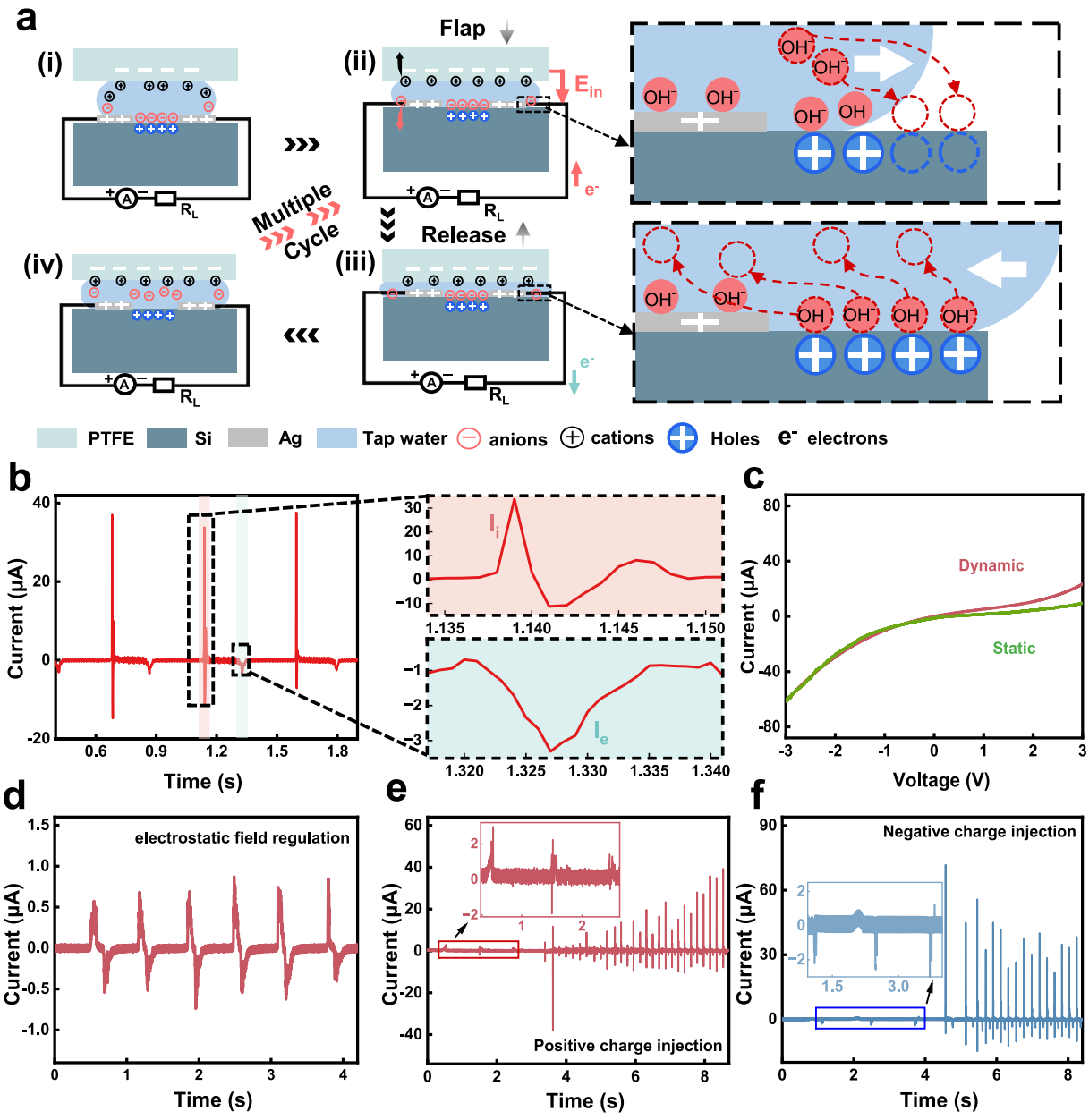

Fig. 4. (a) Working mechanism of tribo-iontronics. (b) Current signal during contact-separation and magnified view. (c) I-V curves under dynamic and static conditions. (d) Schematic of charge injection using an electrostatic gun. (e-f) Current profiles after injecting positive and negative charges.

interfaces, respectively. The comparable work functions of n-Si and Ag indicate that both interfaces can participate in interfacial charge redistribution (Fig. S21a) [40]. Water adsorption modifies the surface potentials of n-Si and Ag and establishes an interfacial potential difference, providing the basis for directional charge transport under dynamic mechanical excitation. The full working cycle is illustrated in Figs. 4a(i)-4a(iv). In the initial stationary state shown in Fig. 4a(i), stable negative charges remain on the PTFE surface. Cations in the water tend to approach the PTFE/water interface, whereas anions tend to approach the water/n-Si interface. At this stage, the interfacial electric double layers remain approximately equilibrated, and the charge distribution is relatively stable. Therefore, almost no current flows through the external circuit. When the PTFE film moves downward and compresses the confined water layer, as shown in Fig. 4a(ii), the charge densities of the electric double layers at the PTFE/water and water/n-Si interfaces rapidly increase, corresponding to a dynamic interfacial charging process. The cations become more densely accumulated near the PTFE/water interface, whereas the anions accumulate near the water/n-Si interface [41,42]. As the interfacial anion density increases, the hole concentration at the n-Si surface also increases, resulting in the formation of more electrostatically coupled anion-hole pairs. The increased hole concentration changes the surface potential of n-Si and generates a transient potential difference between n-Si and the Ag electrodes. To restore charge equilibrium, electrons migrate from n-Si toward the Ag electrodes and subsequently flow into the external circuit, thereby producing the dominant forward current I_i. When the external force is released and the PTFE film rebounds upward, as illustrated in Fig. 4a (iii), the confined water film contracts, and the interfacial electric double layers undergo a discharging process. The deformation and return flow of the water film remove and redistribute some of the anions previously enriched near the water/n-Si interface, thereby decreasing the local interfacial anion density [43]. Consequently, the number of electrostatically coupled anion-hole pairs decreases, and the hole concentration at the n-Si surface is reduced. The previously established potential difference therefore gradually diminishes. To restore the initial charge equilibrium, electrons flow in the direction opposite to that during compression, producing a weaker reverse current I_e in the external circuit [44,45]. As the water film gradually recovers its initial morphology in Fig. 4a(iv), the cations and anions return toward their initial quasi-equilibrium distributions. Meanwhile, the hole concentration and surface potential of n-Si gradually recover to their initial levels. Consequently, the external current decreases to zero, and the device enters the next compression-rebound cycle [46,47]. The band structure before PTFE contacts n-Si is shown in Fig. S21b(i). The n-Si substrate forms ohmic contact with the bottom silver electrode, and the entire system remains near thermodynamic equilibrium. After one full contact-separation cycle shown in Fig. S21b(ii), electron transfer from n-Si to PTFE generates a triboelectric field (E_{tribo}), which bends the energy bands near the silicon surface and reinforces the built-in electric field. This observation verifies that triboelectric potential modulates the semiconductor band alignment, which is the core mechanism enabling non-equilibrium DC output [48,49]. During compression, dynamic EDL charging and the increased formation of anion–hole pairs generate a strong and rapid positive current pulse I_i. During rebound, EDL discharging, anion redistribution, and interfacial potential relaxation produce a weaker and shorter reverse current I_e (Fig. 4b). Fig. S22 compares current-voltage (I-V) curves measured with and without the water film. The presence of water greatly increases the current output and steepens the I-V slope. These changes indicate that the interfacial water film enhances electrical conductance and reduces the effective resistance to interfacial charge transfer. A further comparison between static and dynamic I-V responses is given in Fig. 4c. During 1 to 3 s of continuous contact and separation, the dynamic curve shifts distinctly upward. This upward shift indicates that dynamic interfacial polarization further reduces the effective resistance to charge transfer and facilitates directional carrier transport. Such dynamic interfacial modulation is difficult to capture by conventional static electrical tests. Consistent trends measured from the top and bottom electrodes confirm that water-induced interface modification widely enhances carrier transport across different electrode junctions. External charge injection tests were performed to clarify how interfacial charge affects interfacial charge transport under water loading. An electrostatic gun was used to inject positive and negative charges onto the device surface. Fig. 4d summarizes the resulting current responses. Positive charge injection onto PTFE first produces a sharp negative current pulse, followed by recovery toward a positive signal, as shown in Fig. 4e. By contrast, negative charge injection triggers an initial positive pulse before gradual recovery (Fig. 4f). Charges accumulated at the PTFE-water interface create a local electric field that penetrates into the underlying semiconductor, thereby changing the local interfacial potential distribution and the effective resistance to charge transfer [50]. Positive and negative charge injection induces opposite interfacial electrostatic perturbations, thereby generating current pulses of opposite polarities. These observations demonstrate that the polarity and density of the surface charges dynamically regulate interfacial charge redistribution and carrier transport. The slow current recovery arises from gradual charge relaxation on the PTFE surface. These results confirm that triboelectric charges in the S–L–S structure dynamically modify the interfacial potential and reduce or increase the effective resistance to charge transfer depending on their polarity, thereby regulating the DC output [51,52].

3.5. *Multifunctional application based on water-solid Interface EDL induced semiconductor non-equilibrium effect direct current output*

Although the EDL-SNE-TENG inherently produces unidirectional DC pulses and can directly drive light-emitting diodes (LEDs) without any rectification (Fig. 5a), a weak reverse current pulse appears during the separation phase (Fig. 4b), which may slightly reduce the charging efficiency when charging external capacitors. To eliminate this effect and obtain a pure charging profile, a rectifier bridge was optionally connected in series with the device (Fig. 5b) [53]. The bridge blocks the reverse leakage current without altering the forward DC output. Charging tests on 0.1 μF, 0.47 μF and 4.7 μF capacitors demonstrate that the charging rate decreases with increasing capacitance, reflecting the intrinsic output characteristics of the EDL-SNE-TENG. While the device achieves stable output under periodic contact-separation motion, dynamic signal response under continuous sliding operation is essential for practical implementation.

Parallel silver electrodes spaced 1 cm apart were fabricated on a 4-in. n-Si wafer, and a water-coated PTFE film was adopted for sliding tests (Fig. 5c). When the water film sweeps across the electrode interval, the interfacial EDLs trigger contact charge variation and induce non-equilibrium carrier migration within the semiconductor. This transient conductive path generates prominent current pulses, verifying that the water film acts as a dynamic charge bridge to sustain stable DC output during sliding. The EDL-SNE-TENG maintains high electrical conductivity and exhibits an asymmetric I-V response under continuous sliding (Fig. 5d). The external circuit acquires regular DC current pulses during rapid sliding of the PTFE-water composite structure (Fig. 5e, Figs. S23 and S24), with stable voltage and charge responses provided in Fig. S25. The underlying mechanism for sliding-induced DC generation is consistent with that of recently reported field-effect nanogenerators [54]. A simplified electrode configuration further verifies device reliability and operational generality. A water-attached PTFE sheet is placed between two silver electrodes, and periodic mild compression creates cyclic contact-separation behavior (Fig. 5f). Cyclic deformation and rebound of the water layer enable repeated formation and breakdown of the S-L-S three-phase interface. In Fig. 5g, the current signal remains stable within the initial 5 s without external compression, while obvious current pulses are captured during the 5 to 10 s pressing-releasing cycles. Even with this simplified structure, the device maintains efficient DC generation based on the electric double layer-induced

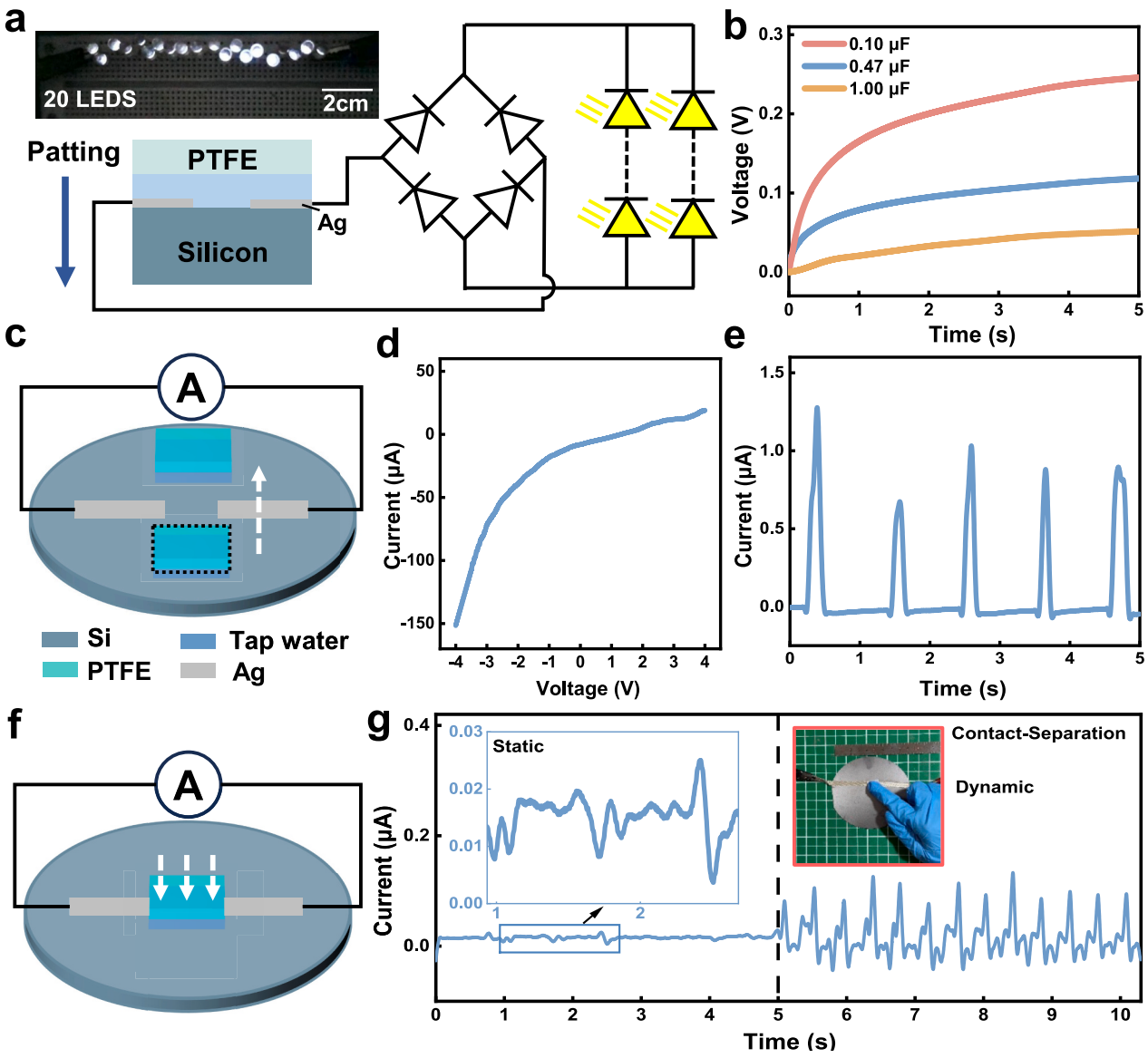

Fig. 5. (a) Photograph and circuit of 20 LEDs driven at 5 Hz. (b) Charging curves of commercial capacitors. (c) Schematic of large-area sliding mode. (d) I-V curve under sliding. (e) Current signal under sliding. (f) Schematic of large-area contact-separation. (g) Current signal under large-area contact-separation.

semiconductor non-equilibrium effect. This indicates that the proposed working principle possesses excellent generality and structural adaptability for diverse device configurations [55].

4. Conclusion

In summary, we have developed an efficient DC micropower harvester based on a S-L-S heterostructure, denoted as the EDL-SNE-TENG, and systematically elucidated the interplay between EDL behavior and semiconductor band modulation. Under cyclic mechanical compression, interfacial water dipoles undergo ordered alignment, generating a strong local electric field. This field reduces the effective work function of n-Si to a stabilized threshold of 4.02 eV and sustains continuous non-equilibrium carrier transport, thereby enabling rectifier-free DC output. The optimized device delivers an open-circuit voltage of 6.5 V, a short-circuit current of 35 μA, and a peak power density of 0.54 $W{\cdot}m^{-2}$, representing an over 50-fold enhancement compared with conventional open-interface TVNGs. This study advances the fundamental understanding of fluidic-gated DC energy harvesting and provides a practical and promising route for powering self-powered microsystems, wearable electronics and Internet-of-Things devices. Further efforts will focus on large-scale array integration, exploration of wide-bandgap semiconductors and in situ spectroscopic characterization of polarized interfacial water to deepen mechanistic insight and boost device performance.

CRediT authorship contribution statement

Sheng-Jie Lin: Writing – review & editing, Writing – original draft, Resources. **Jiang-Tao Guo:** Writing – review & editing, Investigation. **Xin-Long Xiao:** Software, Formal analysis. **Wen Yang:** Supervision, Investigation. **Yun-Bo Zhang:** Investigation, Funding acquisition. **Yong Zhang:** Writing – review & editing, Resources. **Pei-Zhi Yang:** Writing – review & editing, Supervision, Funding acquisition.

Declaration of competing interest

The authors declare that they have no known competing financial interests or personal relationships that could have appeared to influence the work reported in this paper.

Acknowledgment

This work was supported by Yunnan Provincial Science and Technology Project at Southwest United Graduate School (Grant No. 202302A0370009), National Natural Science Foundation of China (No. U1802257), Yunnan Revitalization Talent Support Program, the Spring City Plan: The High-level Talent Promotion and Training Project of Kunming (2022SCP005), Project for Building a Science and Technology Innovation Center Facing South Asia and Southeast Asia (202403AP140015).

Appendix A. Supplementary data

Supplementary data to this article can be found online at https://doi.org/10.1016/j.cej.2026.181339.

Data availability

Data will be made available on request.

References

[1] S. Lin, L. Xu, A.C. Wang, Z.L. Wang, Quantifying electron-transfer in liquid-solid contact electrification and the formation of electric double-layer, Nat. Commun. 11 (2020) 399, https://doi.org/10.1038/s41467-019-14278-9.
[2] C. Chen, S. Zhao, C. Pan, Y. Zi, F. Wang, C. Yang, Z.L. Wang, A method for quantitatively separating the piezoelectric component from the as-received "piezoelectric" signal, Nat. Commun. 13 (2022) 1391, https://doi.org/10.1038/s41467-022-29087-w.
[3] Y. Zou, P. Tan, B. Shi, H. Ouyang, D. Jiang, Z. Liu, H. Li, M. Yu, C. Wang, X. Qu, L. Zhao, Y. Fan, Z.L. Wang, Z. Li, A bionic stretchable nanogenerator for underwater sensing and energy harvesting, Nat. Commun. 10 (2019) 2695, https://doi.org/10.1038/s41467-019-10433-4.
[4] H. Zhao, M. Xu, M. Shu, J. An, W. Ding, X. Liu, S. Wang, C. Zhao, H. Yu, H. Wang, C. Wang, X. Fu, X. Pan, G. Xie, Z.L. Wang, Underwater wireless communication via TENG-generated Maxwell's displacement current, Nat. Commun. 13 (2022) 3325, https://doi.org/10.1038/s41467-022-31042-8.
[5] H. Wang, L. Xu, Y. Bai, Z.L. Wang, Pumping up the charge density of a triboelectric nanogenerator by charge-shuttling, Nat. Commun. 11 (2020) 4203, https://doi.org/10.1038/s41467-020-17891-1.
[6] Q. Sun, F. Liang, G. Ren, L. Zhang, S. He, K. Gao, Z. Gong, Y. Zhang, X. Kang, C. Zhu, Density-of-states matching-induced ultrahigh current density and high-humidity resistance in a simply structured triboelectric nanogenerator, Adv. Mater. 35 (14) (2023) 2210915, https://doi.org/10.1002/adma.202210915.
[7] H. Zhou, X. Wang, M. Wang, J. He, Y. Nan, L. Yang, L. Luo, J. Duan, Hydrostatic pressure contact improves the performance of triboelectric nanogenerators, Adv. Funct. Mater. 36 (42) (2026) e74841, https://doi.org/10.1002/adfm.74841.
[8] S. Liu, S. An, X. Zhou, J. Wang, X. Pu, A self-powered, process-oriented wireless sensor with high discharge signal density, Device 2 (9) (2024) 100437, https://doi.org/10.1016/j.device.2024.100437.
[9] X. Huang, X. Xiang, J. Nie, D. Peng, F. Yang, Z. Wu, H. Jiang, Z. Xu, Q. Zheng, Microscale Schottky superlubric generator with high direct-current density and ultralong life, Nat. Commun. 12 (1) (2021) 2268, https://doi.org/10.1038/s41467-021-22371-1.
[10] Y. Yu, H. Li, X. Zhang, Q. Gao, B. Yang, Z.L. Wang, T. Cheng, Substantially boosting performance of triboelectric nanogenerators via a triboelectrification enhancement effect, Joule 8 (6) (2024) 1855–1868, https://doi.org/10.1016/j.joule.2024.04.013.
[11] H. Wang, X. Xia, J. Fu, J. Li, C. Chen, Y. Dai, Z. Fan, G. Hu, Y. Zi, A general self-powered wireless sensing solution based on triboelectric-discharge effect, Nano Energy 105 (2023) 107982, https://doi.org/10.1016/j.nanoen.2022.107982.
[12] Z. Liu, S. Lin, P. Yang, S. Qin, J. Hu, X. Chen, A wiping-type semiconductor–liquid generator utilizing water-bearing solid materials and hydrated biological tissues, Energy Environ. Sci. 17 (18) (2024) 6582–6593, https://doi.org/10.1039/D4EE02797C.
[13] M. Shah, S. Li, Z. Yang, J. Liu, P. Peng, H. Qian, Z.L. Wang, D. Wei, Synergistic effects in triboelectric charge-driven redox reactions, Nano Energy 144 (2025) 111380, https://doi.org/10.1016/j.nanoen.2025.111380.
[14] W. He, W. Liu, S. Fu, H. Wu, C. Shan, Z. Wang, Y. Xi, X. Wang, H. Guo, H. Liu, C. Hu, Ultrahigh performance triboelectric nanogenerator enabled by charge transmission in interfacial lubrication and potential decentralization design, Research 2022 (2022) 9812865, https://doi.org/10.34133/2022/9812865.
[15] Y. Li, Q. Zhang, Y. Cao, Z. Kang, H. Ren, Z. Hu, M. Gao, X. Ma, J. Yao, Y. Wang, A constant-current generator via water droplets driving Schottky diodes without a rectifying circuit, Energy Environ. Sci. 16 (10) (2023) 4620–4629, https://doi.org/10.1039/D3EE02280C.
[16] R. Zhang, M. Hummelgård, Y. Xu, M. Olsen, J. Örtegren, G. Thungström, H. Andersson, Z.L. Wang, Harnessing dynamic electrostatic fields for energy generation with diode cells, Adv. Sci. 12 (28) (2025) e05476, https://doi.org/10.1002/advs.202505476.
[17] Y. Lu, Y. Yan, X. Yu, X. Zhou, S. Feng, C. Xu, H. Zheng, Z. Yang, L. Li, K. Liu, S. Lin, Polarized water driven dynamic PN junction-based direct-current generator, Research 2021 (2021) 7505638, https://doi.org/10.34133/2021/7505638.
[18] W. He, C. Shan, S. Fu, H. Wu, J. Wang, Q. Mu, G. Li, C. Hu, Large harvested energy by self-excited liquid suspension triboelectric nanogenerator with optimized charge transportation behavior, Adv. Mater. 35 (7) (2023) 2209657, https://doi.org/10.1002/adma.202209657.
[19] C. Bai, X. Li, X. Cui, X. Yang, X. Zhang, K. Yang, T. Wang, H. Zhang, Transparent stretchable thermogalvanic PVA/gelation hydrogel electrolyte for harnessing solar energy enabled by a binary solvent strategy, Nano Energy 100 (2022) 107449, https://doi.org/10.1016/j.nanoen.2022.107449.
[20] R. Guo, Q. Feng, K. Ma, G.-H. Lee, M. Jamal, X. Zhao, K.C. Bustillo, J. Wan, D. S. Ritchie, L. Shan, Memsensing by surface ion migration within Debye length, Nat. Mater. 25 (1) (2026) 18–25, https://doi.org/10.1038/s41563-025-02312-9.
[21] R.R. Sahu, A.S. Ramasamy, S. Bhonsle, M. Vailshery, A. S, H. Kumar, T. Das Gupta, Single-step fabrication of liquid gallium nanoparticles via capillary interaction for dynamic structural colours, Nat. Nanotechnol. 19 (6) (2024) 766–774, https://doi.org/10.1038/s41565-024-01625-1.
[22] S. Wang, L. Han, Y. Zou, B. Liu, Z.-h. He, Y. Huang, Z. Wang, L. Zheng, Y.-x. Hu, Q. Zhao, Ultrahigh-gain organic transistors based on van der Waals metal-barrier interlayer-semiconductor junction, Sci. Adv. 9 (49) (2023) eadj4656, https://doi.org/10.1126/sciadv.adj4656.
[23] O. Demircioglu, M.O. Cicek, D. Doganay, G. Gazaloglu, C. Baykal, S. Cinar, H. E. Unalan, Triboelectric nanogenerators for blue energy harvesting in simulated wave conditions, Nano Energy 107 (2023) 108157, https://doi.org/10.1016/j.nanoen.2023.108157.
[24] J. Meng, G. Zhang, L. Pang, Q. Liu, J. Yao, Y. Wang, H. Liu, C. Guo, W. Bao, J. Li, Zinc–bromine batteries revisited: unlocking liquid-phase redox chemistry for next-generation energy storage, Energy Environ. Sci. 18 (20) (2025) 9031–9053, https://doi.org/10.1039/D5EE02219C.
[25] X. Li, Z.L. Wang, D. Wei, Scavenging energy and information through dynamically regulating the electrical double layer, Adv. Funct. Mater. 34 (42) (2024) 2405520, https://doi.org/10.1002/adfm.202405520.
[26] H. Wang, X. Xia, J. Fu, Z. Song, W. Ding, Y. Dai, Y. Zi, A flexible lightweight self-powered wireless metal detector enabled by triboelectric discharge effect, Device 1 (6) (2023) 100127, https://doi.org/10.1016/j.device.2023.100127.
[27] M. Zheng, S. Lin, Z. Tang, Y. Feng, Z.L. Wang, Photovoltaic effect and tribovoltaic effect at liquid-semiconductor interface, Nano Energy 83 (2021) 105810, https://doi.org/10.1016/j.nanoen.2021.105810.
[28] W. He, Y. Liu, J. Jin, J. Cai, B. Wan, J. Chen, X. Yang, C. Hu, High durability sliding TENG with enhanced output achieved by capturing multiple region charges for harvesting wind energy, Nano Micro Lett. 18 (1) (2026) 199, https://doi.org/10.1007/s40820-025-02043-1.
[29] S. Li, Z. Zhang, F. Yang, X. Li, P. Peng, Y. Du, Q. Zeng, M. Willatzen, Z.L. Wang, D. Wei, Transistor-like triboiontronics with record-high charge density for self-powered sensors and neurologic analogs, Device 2 (6) (2024) 100332, https://doi.org/10.1016/j.device.2024.100332.
[30] C. Chen, J. Nie, J. An, X. Xia, Z. Wu, H. Wang, H. Cui, Q. Zheng, Y. Zi, Microscale contact electrification with unprecedented high intrinsic charge density, Small 21 (39) (2025) e06466, https://doi.org/10.1002/smll.202506466.
[31] X. Li, R. Li, S. Li, Z.L. Wang, D. Wei, Triboiontronics with temporal control of electrical double layer formation, Nat. Commun. 15 (1) (2024) 6182, https://doi.org/10.1038/s41467-024-50518-3.
[32] X. Li, Y. Wei, X. Gao, Z. Zhang, Z.L. Wang, D. Wei, Harnessing triboiontronic Maxwell's demon by triboelectric-induced polarization for efficient energy-information flow, Joule 9 (5) (2025) 101888, https://doi.org/10.1016/j.joule.2025.101888.
[33] Y. Gao, L. He, D. Liu, J. Zhang, L. Zhou, Z.L. Wang, J. Wang, Spontaneously established reverse electric field to enhance the performance of triboelectric nanogenerators via improving coulombic efficiency, Nat. Commun. 15 (1) (2024) 4167, https://doi.org/10.1038/s41467-024-48456-1.
[34] C. Ma, B. Kim, D.-H. Kang, S.-W. Kim, N.-G. Park, Nonchemical n-and p-type charge transfer doping of FAPbI3 perovskite, ACS Energy Lett. 6 (8) (2021) 2817–2824, https://doi.org/10.1021/acsenergylett.1c01233.
[35] Y. Hu, W. Yang, Y. Ma, Y. Qiu, W. Wei, B. Wu, K. Li, Y. Li, Q. Zhang, R. Xiao, Solid-liquid interface charge transfer for generation of H_2O_2 and energy, Nat. Commun. 16 (1) (2025) 1692, https://doi.org/10.1038/s41467-025-57082-4.
[36] Y. Li, H. Ren, Z. Hu, Z. Hu, J. Wang, M. Zhang, Y. Yu, S. Chen, Z.L. Wang, Z. Yang, Schottky MSM-structured tribovoltaic nanogenerator enabling over 25,000 nC charge transfer via single droplet impact, Adv. Mater. 37 (33) (2025) 2504902, https://doi.org/10.1002/adma.202504902.
[37] L. Xie, B. Lu, Z. Sima, Y. Liu, H. Ji, Z. Gao, P. Jiang, H. Van Zalinge, I.Z. Mitrovic, X. Sun, Mechanical–electric dual characteristics solid–liquid interfacing sensor for accurate liquid identification, Nat. Commun. 16 (1) (2025) 7069, https://doi.org/10.1038/s41467-025-62524-0.
[38] X. Xu, Z.L. Wang, Z. Yang, Triboelectric junction: a model for dynamic metal–semiconductor contacts, Energy Environ. Sci. 17 (1) (2024) 149–157, https://doi.org/10.1039/D3EE02870D.
[39] Q.T. Nguyen, T. Van Tam, D.L. Vu, J.H. Ahn, W.M. Choi, K.K. Ahn, Ultrahigh current density DC triboelectric generator for energy harvesting and self-powered sensing, Nano Energy 143 (2025) 111291, https://doi.org/10.1016/j.nanoen.2025.111291.
[40] H. Xiao, Z. Yu, J. Liang, L. Ding, J. Zhu, Y. Wang, S. Chen, J.H. Xin, Wetting behavior-induced interfacial transmission of energy and signal: materials,

mechanisms, and applications, Adv. Mater. 36 (36) (2024) 2407856, https://doi.org/10.1002/adma.202407856.
[41] H. Qin, L. Xu, S. Lin, F. Zhan, K. Dong, K. Han, H. Wang, Y. Feng, Z.L. Wang, Underwater energy harvesting and sensing by sweeping out the charges in an electric double layer using an oil droplet, Adv. Funct. Mater. 32 (18) (2022) 2111662, https://doi.org/10.1002/adfm.202111662.
[42] J. Nauruzbayeva, Z. Sun, A. Gallo Jr., M. Ibrahim, J.C. Santamarina, H. Mishra, Electrification at water–hydrophobe interfaces, Nat. Commun. 11 (1) (2020) 5285, https://doi.org/10.1038/s41467-020-19054-8.
[43] J. Li, Y. Li, L. Ma, Y. Tian, Streaming potential effect in droplet electricity generator, Nano Energy (2026) 112249, https://doi.org/10.1016/j.nanoen.2026.112249.
[44] W. Xu, H. Zheng, Y. Liu, X. Zhou, C. Zhang, Y. Song, X. Deng, M. Leung, Z. Yang, R. X. Xu, A droplet-based electricity generator with high instantaneous power density, Nature 578 (7795) (2020) 392–396, https://doi.org/10.1038/s41586-020-1985-6.
[45] Y. Zhao, L. Wang, G. Li, C. Rao, Y. Pan, B. Chen, H. Xu, F. Mugele, H. Wu, Boosting the charge output of enclosed liquid-based nanogenerators by electrowetting-assisted charge injection approach, Adv. Sci. 12 (38) (2025) e06517, https://doi.org/10.1002/advs.202506517.
[46] Z.-H. Lin, G. Cheng, S. Lee, K.C. Pradel, Z.L. Wang, Harvesting water drop energy by a sequential contact-electrification and electrostatic-induction process, Adv. Mater. 26 (27) (2014) 4690–4696, https://doi.org/10.1002/adma.201400373.
[47] X. Li, P. Bista, A.Z. Stetten, H. Bonart, M.T. Schür, S. Hardt, F. Bodziony, H. Marschall, A. Saal, X. Deng, Spontaneous charging affects the motion of sliding drops, Nat. Phys. 18 (6) (2022) 713–719, https://doi.org/10.1038/s41567-022-01563-6.
[48] R. Yang, M. Benner, Z. Guo, C. Zhou, J. Liu, High-performance flexible Schottky DC generator via metal/conducting polymer sliding contacts, Adv. Funct. Mater. 31 (43) (2021) 2103132, https://doi.org/10.1002/adfm.202103132.
[49] H. Wu, Y. Li, Q. Wan, H. Deng, J. Qin, J. Tang, X. Zhang, S. Xiao, From liquid–solid contact electrification to triboelectric nanogenerators: mechanism, methods and applications, Adv. Energy Mater. 16 (6) (2026) e05772, https://doi.org/10.1002/aenm.202505772.
[50] M. Zheng, S. Lin, L. Xu, L. Zhu, Z.L. Wang, Scanning probing of the tribovoltaic effect at the sliding interface of two semiconductors, Adv. Mater. 32 (21) (2020) 2000928, https://doi.org/10.1002/adma.202000928.
[51] J. Guo, L. Duan, W. Yang, Q. Wang, X. Feng, Y. Zhang, Y. Zhang, Z.L. Wang, P. Yang, Flexible triboelectric nanogenerator arrays for energy harvesting and direct current output via solid-liquid-gas interfaces involving liquid metals, Adv. Funct. Mater. 35 (49) (2025) e10233, https://doi.org/10.1002/adfm.202510233.
[52] Q. Zhang, Y. Li, H. Cai, M. Yao, H. Zhang, L. Guo, Z. Lv, M. Li, X. Lu, C. Ren, A single-droplet electricity generator achieves an ultrahigh output over 100 V without pre-charging, Adv. Mater. 33 (51) (2021) 2105761, https://doi.org/10.1002/adma.202105761.
[53] L. Xu, E. Wang, Y. Kang, D. Fu, L. Luo, Y. Quan, Y. Xi, J. Huang, X. Cui, J. Zeng, D. Jiang, B. Shi, H. Feng, H. Ouyang, C. Chen, Z. Li, Schottky nanodiodes array enabled triboelectric nanosecond pulse generator for ultralow-cost tumor therapy, Device 3 (6) (2025) 100721, https://doi.org/10.1016/j.device.2025.100721.
[54] C. Pan, L.N. Cao, J. Meng, L. Jia, W. Hu, Z.L. Wang, X. Pu, Field effect nanogenerator operated by sliding gates, Energy Environ. Sci. 17 (3) (2024) 1132–1140, https://doi.org/10.1039/D3EE03496H.
[55] W. Wang, Y. Jiang, D. Zhong, Z. Zhang, S. Choudhury, J.-C. Lai, H. Gong, S. Niu, X. Yan, Y. Zheng, Neuromorphic sensorimotor loop embodied by monolithically integrated, low-voltage, soft e-skin, Science 380 (6646) (2023) 735–742, https://doi.org/10.1126/science.ade0086.